

Visualizing Reaction Fronts and Transport Limitations in Solid-State Li–S Batteries via Operando Neutron Imaging

Robert Bradbury, Georg F. Dewald, Marvin A. Kraft, Tobias Arlt, Nikolay Kardjilov, Jürgen Janek, Ingo Manke,* Wolfgang G. Zeier,* and Saneyuki Ohno*

The exploitation of high-capacity conversion-type materials such as sulfur in solid-state secondary batteries is a dream combination for achieving improved battery safety and high energy density in the push toward a sustainable future. However, the exact reason behind the low rate-capability, bottlenecking further development of solid-state lithium–sulfur batteries, has not yet been determined. Here, using neutron imaging, the spatial distribution of lithium during cell operation is directly visualized and it is shown that sluggish macroscopic ion transport within the composite cathode is rate-limiting. Observing a reaction front propagating from the separator side toward the current collector confirms the detrimental influence of a low effective ionic conductivity. Furthermore, irreversibly concentrated lithium in the vicinity of the current collector, revealed via state-of-charge-dependent tomography, highlights a hitherto-overlooked loss mechanism triggered by sluggish effective ionic transport within a composite cathode. This discovery can be a cornerstone for future research on solid-state batteries, irrespective of the type of active material.

and natural abundance of sulfur-active material,^[3,4] solid-state Li–S batteries have the potential to cause a paradigm shift through simultaneous enhancement of long-term stability and battery safety, together with boosted energy density (Wh kg⁻¹).^[5] Nevertheless, solid-state Li–S batteries do not yet fulfil performance expectations, and further improvement is required.^[6] Electrochemical reactions require a low-impedance supply of ions and electrons but sulfur-active materials are ionically and electronically insulating. Hence, for a functional cathode, the sulfur-active materials need to be composited with ion and electron conductive additives. These composites provide sufficient triple-phase boundaries where consecutive conversion reactions take place in which the active material can receive or donate ions and electrons.^[7] As a result, a functional sulfur cathode often contains a high

interfacial area per unit volume (>10⁴–10⁶ cm⁻¹).^[8]

In particular, the rate-limiting step in solid-state Li–S batteries is, at present, not well understood. Despite the very short diffusion length and the substantial numbers of triple-phase boundaries created after the compositing procedure, slow diffusion of charge carriers in sulfur-active materials^[9] and high-impedance charge transfer over the electrolyte-active material

1. Introduction

Solid-state batteries offer the potential for greater energy densities and increased safety and are therefore currently discussed as an alternative to lithium-ion batteries.^[1,2] By combining the concepts of solid-state batteries with conversion-type lithium–sulfur (Li–S) cells that have a high theoretical specific energy

R. Bradbury, T. Arlt
Institute for Materials Science and Technologies
Technische Universität Berlin
Straße des 17. Juni 135, 10623 Berlin, Germany

R. Bradbury, N. Kardjilov, I. Manke
Helmholtz-Zentrum Berlin für Materialien und Energie (HZB)
Hahn Meitner Platz 1, D-14109 Berlin, Germany
E-mail: manke@helmholtz-berlin.de

G. F. Dewald, J. Janek
Institute of Physical Chemistry
Justus-Liebig-University Gießen
Heinrich-Buff-Ring 17, D-35392 Gießen, Germany

 The ORCID identification number(s) for the author(s) of this article can be found under <https://doi.org/10.1002/aenm.202203426>.

© 2023 The Authors. Advanced Energy Materials published by Wiley-VCH GmbH. This is an open access article under the terms of the Creative Commons Attribution License, which permits use, distribution and reproduction in any medium, provided the original work is properly cited.

DOI: 10.1002/aenm.202203426

G. F. Dewald, J. Janek
Center for Materials Research (LaMa)
Justus-Liebig-University Gießen
Heinrich-Buff-Ring 16, D-35392 Gießen, Germany

M. A. Kraft, W. G. Zeier
Institut für Energie- und Klimaforschung (IEK)
IEK-12: Helmholtz-Institut Münster
Forschungszentrum Jülich
48149 Münster, Germany

W. G. Zeier
Institute of Inorganic and Analytical Chemistry
University of Münster
Correnstrasse 30, 48149 Muenster, Germany
E-mail: wzeier@uni-muenster.de

S. Ohno
Department of Applied Chemistry
Graduate School of Engineering
Kyushu University
744 Motoooka, Nishi-ku, Fukuoka 819-0395, Japan
E-mail: saneyuki.ohno@cstf.kyushu-u.ac.jp

interfaces^[10] have often been cited as the rate-limiting steps.^[11] In contrast, the sluggish ion transport within the composite itself, which becomes exponentially worse at high potential, strongly contributes to a high overpotential.^[8] This retarded ion transport is not limited to solid-state Li–S batteries and the same transport limitations within the cathode composite are found in intercalation-type solid-state batteries.^[12,13] In other words, irrespective of the cathode-active material used, a low effective ionic conductivity of the cathode composite may be the bottleneck for solid-state battery development. Electrochemical impedance spectroscopy can provide details on the ionic transport. However, a visualization of the overall spatial distribution of transport limitations is essential for determining critical bottlenecks toward high-loading and thick cathode design, as well as fast charging/discharging. Thus, the development of a technique that can monitor cells operando and visualize the distribution of lithium is needed.^[14]

Notably, progress in the field of X-ray imaging allowed for the elucidation of solid-state batteries while under operation.^[15–18] Since X-ray attenuation coefficients monotonically increase with atomic number, the identification of lithium, a light element, using X-rays is challenging. Here, neutron-based techniques appear promising due to the high neutron attenuation of lithium compared to other elements that comprise the cathode composite. Neutron radiography has been successfully employed in the characterization of batteries with liquid electrolytes^[19–21] as has another nondestructive technique, neutron depth profiling.^[22–24] In solid systems, operando neutron diffraction has been conducted to investigate the crystallization of solid electrolytes and lithium transport in garnet-based solid-state cells via depth profiling.^[25,26] To the best of our knowledge, operando neutron analysis has not yet, to date, been performed on solid-state batteries.

2. Results and Discussion

In order to perform the operando neutron analysis on the solid-state cell, a cell housing made from aluminium, with a hollow

interior was developed, as depicted in **Figure 1a**. To ensure electrical insulation of the cell, the stack was prepared inside a polyimide tube. The battery components were sandwiched between two stainless steel stamps with O-ring seals to protect the lithium-thiophosphate-based solid-state Li–S battery (In/Li | Li₆PS₅Cl | S/C/Li₆PS₅Cl) from exposure to air and moisture during cycling. A thick cathode configuration delivering an areal capacity of almost 12 mAh cm⁻² was employed to better observe changes in the cathode composite layer (see Figures S1 and S2 in the Supporting Information for details of the cell performance).

The neutron beam transmitted through the cell can visualize the components with the level of contrast determined by the degree of neutron absorption (see Table S1, Supporting Information). **Figure 1b** shows a representative 2D neutron radiograph of the cell before cycling. Darker areas represent the components with low neutron transmission or high absorption. Among the elements comprising the cathode and electrolyte regions, lithium possesses the highest neutron absorption coefficient,^[27] thus the contrast changes are primarily due to the variations in lithium concentration. In the anode, the presence of indium should be noted since it has an even higher neutron absorption coefficient than lithium.^[27] This is reflected in **Figure 1b** where the attenuation of the neutron beam is much greater in the anode. However, since indium remains immobile throughout the electrochemical cycling, mobile lithium can be considered to be responsible for all changes in neutron attenuation. In the pristine state, the attenuation difference between the solid electrolyte and the cathode composite is less distinct than for the anode due to the similar Li environments in both components. However, the additional carbon and sulfur present in the cathode alter the Li density sufficiently to enable the two regions to be differentiated in the radiography images. The neutron attenuation measured in the pristine (as-prepared) and fully discharged cells show distinct differences (**Figure 1c**). These are most evident in the cathode, where the change from the pristine to the fully discharged state is significant. It is consistent with what is occurring in the cell during discharge—there is a net loss in lithium from the anode and a net gain

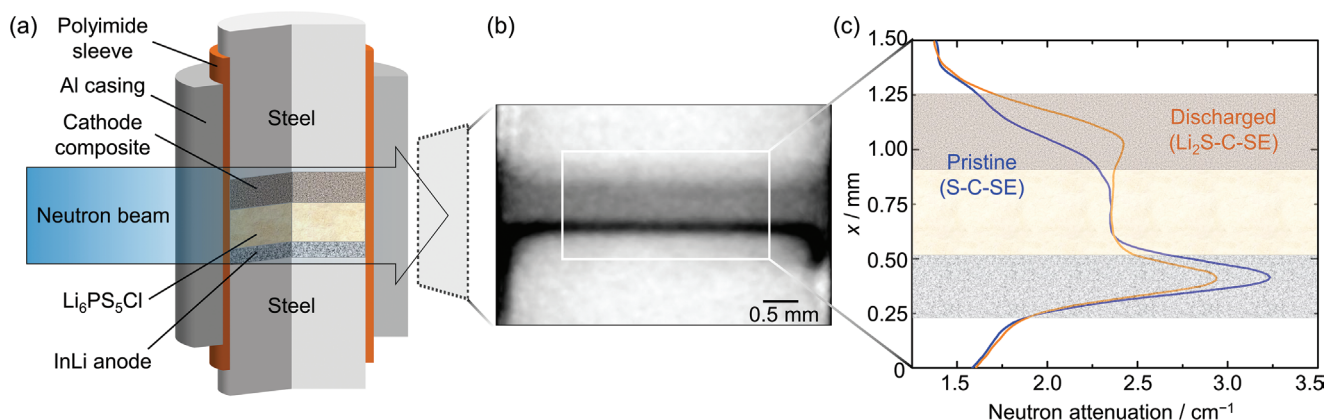


Figure 1. Cell design, representative neutron radiography, and neutron attenuation. a) Schematic representation of the experimental setup for neutron imaging. A custom-made cell optimized for neutron imaging was employed. b) The element-specific neutron attenuation allows differentiation of the cell components from the steel and aluminium in the neutron radiogram. c) The position-dependent neutron attenuation quantified within the white box in (b) before and after the initial discharge visualizes the variation in the distribution of the Li concentration. The plateau seen in the separator giving neutron attenuation of about 2.35 cm⁻¹ shows good agreement with the theoretical value of Li₆PS₅Cl (2.47 cm⁻¹).

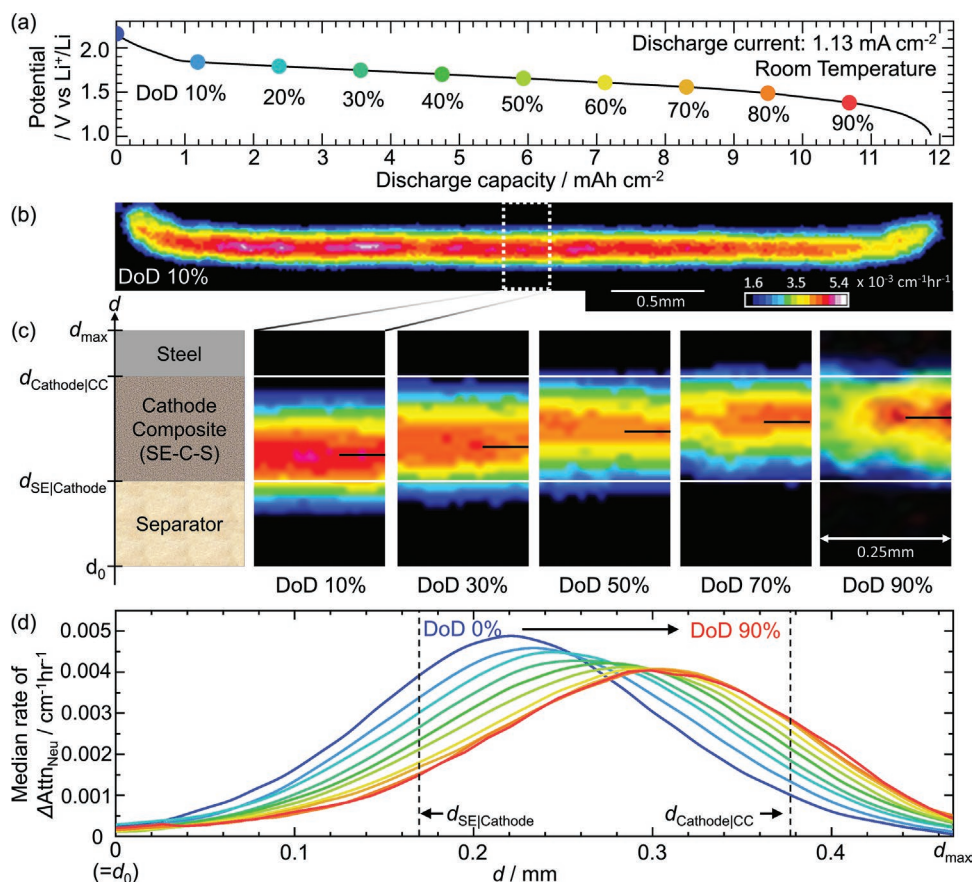


Figure 2. Dynamics of lithium distribution visualized by operando neutron radiography. a) Voltage decrease plotted as a function of discharge capacity. Each data point represents the degree of discharge (DoD). b) Neutron radiography image of the cathode composite at 10% DoD. The color scale represents the rate of change in neutron attenuation with the same limits as (c) and Figure S5 in the Supporting Information. Neutron attenuation and change in neutron attenuation as functions of time are displayed in the Supporting Information (Figures S2 and S3). In the vertical direction, the image ranges from d_0 to d_{max} . c) Progression of the point of maximum rate of attenuation change (reaction front) toward higher d as DoD increases. The region displayed for each DoD is taken from the equivalent dotted area in each image as illustrated in (b) for 10% DoD. The white lines represent the cathode interfaces with the steel current collector (upper) and the solid electrolyte separator (lower), which were determined based on the data at 0% DoD in combination with the 3D tomography data. The black lines correspond to the position giving the maxima median rate of attenuation change in (d). d) Median rate of attenuation change as a function of d (using the full-width data as shown in (b) and Figure S5, Supporting Information). The dotted lines represent the interfaces as denoted by the white lines in (c).

at the cathode, while the solid electrolyte separator exhibits no overall change.

Whereas in situ neutron tomography offers the opportunity to quantify the lithium distribution through the cathode in 3D at specific charge states, 2D radiography, conducted operando, can visualize the changes in lithium distribution through the cathode composite during cathode lithiation/delithiation. The solid-state Li-S cell was cycled at 1.13 mA cm^{-1} while in the neutron beam (Figure 2a). Throughout the initial discharge images were recorded, each with an exposure time of 10 s and a pixel size of 13 μm (see Video S1 and Figure S3, Supporting Information). After processing the images to account for the background and normalizing them to the initial pristine state, what is now represented is the change in the number of transmitted neutrons relative to the initial state. However, since the images are a 2D representation of a cylindrical cell, the path taken by the neutrons (l_p) is not constant across the image. This can be resolved by using the Beer–Lambert law (see the Supporting Information) to convert neutron transmission to attenuation.

Neutron attenuation is dependent on l_p and has units of cm^{-1} . To do this, it is necessary to consider each pixel in the image individually and, working out from the center where l_p is the cell diameter, the path length for each can be calculated using simple trigonometry. Compiling the images together in sequence, it becomes clear how the attenuation changes with time (see Video S2, Supporting Information), with a brighter area, reflecting the local presence of more lithium. In order to focus attention on the cathode composite only, a region between a point in the solid electrolyte separator denoted by d_0 , and a point in the steel current collector, denoted by d_{max} is displayed. Figure S4 in the Supporting Information displays the attenuation change for the cathode at 10% intervals in the depth of discharge (DoD).

If we consider how each pixel changes with time, taking the derivative of the attenuation change offers a clear picture of where the lithium is distributed in the cathode composite and when it arrives, as shown in Video S3 in the Supporting Information. The heatmap in Figure 2b highlighting the rate of neutron attenuation change (change in $\Delta \text{Attr}_{\text{Neu}}$ as a function

of time) shows that there is a distribution through the cathode of the rate at which the attenuation changes. The maximum rate of attenuation change progresses through the cathode with time. Figure 2c shows the propagation of this “reaction front” through the cathode as a function of DoD (the full cathode width images of the rate of change of attenuation are displayed in Figure S5 in the Supporting Information at 10% intervals of DoD). The shift in the maximum rate of change is highlighted in Figure 2d whereby the median rate of attenuation change is displayed as a function of d for 10% DoD intervals. This formation of the reaction front propagating from the separator side toward the current collector was also observed with the thinner cathode configuration as shown in Figures S8–S10 in the Supporting Information. The edges of the cell deform slightly due to the soft polyimide sleeve used for cell insulation. This occurs around the full circumference of the cell but is only clearly visible in Figure 2b for the edges of the cell perpendicular to orientation of the neutron beam. This and the limitation of the instrument resolution are responsible for the broadening of the peak shape as well as spill-over into the region of the steel current collector when $d > d_{\text{Cathode|CC}}$ and the separator when $d < d_{\text{SE|Cathode}}$. Variation in the rate of attenuation change is to be expected across the cell throughout electrochemical cycling but a given point in the cathode composite will experience the greatest rate of change when the lithium front first arrives. Notably, the volume change and the resulting shift in $d_{\text{SE|Cathode}}$

during operando radiography were not trackable due to the limited resolution and above-mentioned deformation. Despite the known volume expansion of the cathode composite upon discharging,^[28] it is clear that this reaction front propagates from the separator-side toward the current collector as the cell discharges.

While operando neutron radiography provides information regarding the dynamics of lithium transport through the cathode composite during cycling, this insight is limited by the 2D nature of the technique, describing the lithium distribution only in terms of d . To acquire information on the homo- or heterogenous distribution in the cathode area for a given d , a different neutron imaging technique, neutron tomography, is required. Although information on the dynamics will be lost since tomography requires a series of images to be recorded as the sample is rotated, these images, taken in situ, can be reconstructed to create a 3D representation of the cell (see Figure S6 in the Supporting Information showing the pristine, discharged, and recharged states).

Through subtraction of the pristine state from subsequently measured tomograms of fully discharged and recharged cells, it is now possible to directly visualize changes to the lithium distribution across the whole volume. Figure 3a shows two 3D representations of the cell, one in a discharged (top) and the other in a charged state (middle). Each tomogram has been normalized to the pristine state to show only the changes in

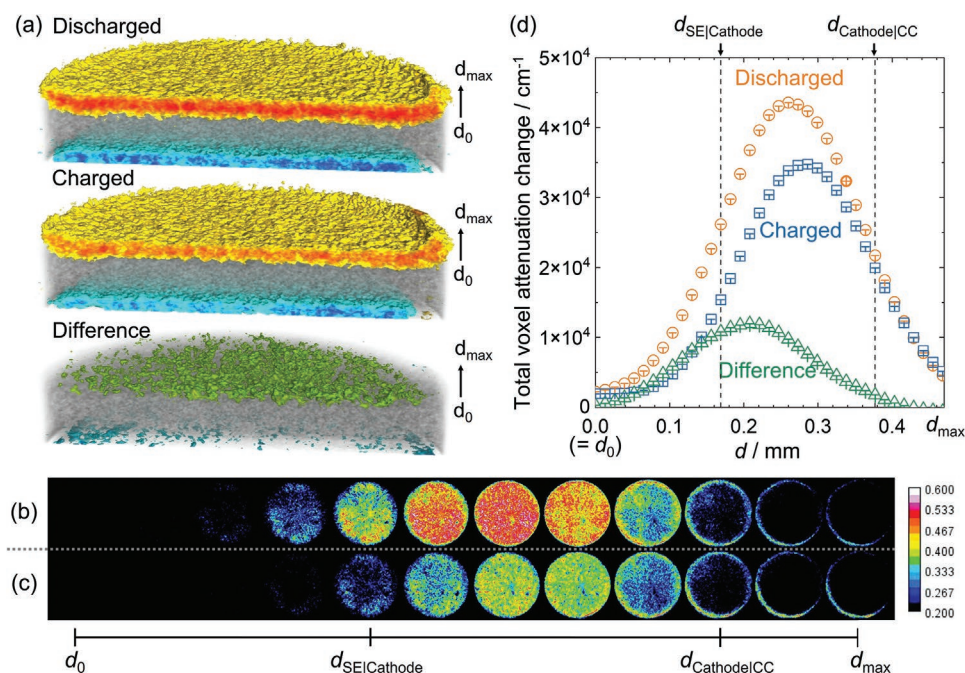


Figure 3. In situ neutron tomography on the discharged and charged solid-state sulfur cathode. a) 3D tomography images of the discharged (top) and recharged state (middle), normalized to the initial state to emphasize changes in the cell (cathode increase in attenuation—yellow to red, anode decrease in attenuation—blue), along with the difference between them (bottom) that shows the location of the mobile lithium (green). b) Median neutron attenuation change through the 200 μm thick cathode composite in the discharged state normalized to the pristine state. The images range from d_0 at the edge of the solid electrolyte region to d_{max} on the current collector side of the cathode composite and each represents a 39 μm thick slice of the cathode. c) Same as (b) but for the recharged state. The color bar in both represents the range of attenuation change above that of the background and is independent of colors used in (a). d) Total neutron attenuation change for 13 μm thick slices through the cathode composite for the discharged (orange) and recharged states (blue). The latter represents the lithium trapped in the cathode. The difference between the two charged states represents the mobile lithium (green). The data are displayed with error bars corresponding to the standard deviation.

the cell affected during cycling. The anode shows the negative attenuation change and the separator region has zero net change in total lithium, similar to the steel stamp below the anode and above the cathode. The separator region is denoted in gray. The cathode, which is the focus of our in-depth analysis, displays a notable difference between the two charge states. This is clearly demonstrated in the third representation (bottom) which shows the difference between the two charge states (the anode difference is less noticeable due to percentage changes to its overall attenuation being much less than the cathode). Figure 3b,c displays the attenuation change in 39 μm thick slices from d_0 to d_{max} for the fully discharged and recharged states, respectively. The difference in attenuation between the discharged and charged states represents the mobile lithium that is stripped from the cathode upon charging. The origin of the nonzero rate of attenuation change observed beyond the cathode|current collector interface in Figure 2d, and attributed to the deformation of the cathode outer edge, is also seen in the final three images in both Figure 3b,c. If we take each image from the series and sum the attenuation change of all voxels within the cell area, the differing behavior across the depth of the cathode composite becomes even clearer (Figure 3d). The discharged state (orange plot) represents the lithium that has accumulated in the cathode upon lithiation of S to form Li_2S during initial discharge. It is evident from Figure 3c,d that the lithium is heterogeneously distributed throughout the cathode. The attenuation from the recharged state (blue plot) represents lithium that is trapped within the cathode composite, in the form of Li_2S that cannot be converted back to S. This trapped lithium is observed across the cathode depth in Figure 3d but is notably greater at higher d , the current collector side of the cathode composite. The mobile lithium that is not trapped in the cathode and which is transported back toward the anode when the cell is recharged can be quantified as the difference between the lithium present in the cathode in the discharged state and that which remains after the cell has been charged. In Figure 3d (green plot), this lithium can be shown to have been located at, and lost from, the solid electrolyte separator side of the cathode composite, at lower d .

Assuming that the cathode composite is homogenous and has a substantially high interfacial area density, we can expand a conventional “1D porous electrode theory,” also known as the Newman model,^[29] to solid-state sulfur cathodes. The model was originally developed to describe the distribution of the reaction current within an electrode that consists of a porous matrix of a reactive material and a liquid electrolyte that had penetrated into voids in the porous material. A dimensionless reaction rate describes the distribution of the reaction current in the thickness direction of the cathode composite, which corresponds to the rate of attenuation change observed in this work. A detailed description can be found in the Supporting Information.

When the effective ionic and electronic conductivities ($\sigma_{\text{ion}}^{\text{eff}}$ and $\sigma_{\text{e}}^{\text{eff}}$) of a cathode composite are sufficiently high with respect to the applied current and thickness, the distribution of reaction current becomes uniform as shown in Figure 4b. With fast supply of ions and electrons, charge transfer and lithium diffusion within the active material particles will remain as potential rate-limiting steps. In contrast, when the effective transport is insufficiently fast, the

reaction current distribution becomes nonuniform, as shown in Figure 4c,d, and the overvoltage due to the sluggish transport within the electrolyte in the composite becomes non-negligible. The degree of nonuniformity is parameterized by

$$\delta \left(= L |I| \beta \left(\frac{1}{\sigma_{\text{ion}}^{\text{eff}}} + \frac{1}{\sigma_{\text{e}}^{\text{eff}}} \right) \right),$$

which is a function of the applied current I , the cathode thickness L , effective conductivities, and a parameter β , which is constant for a given battery chemistry. It is notable that with $\sigma_{\text{e}}^{\text{eff}} \gg \sigma_{\text{ion}}^{\text{eff}}$, the model predicts a nonuniform reaction rate with the formation of a reaction front propagating from the separator-layer side toward the current collector (Figure 4c).^[30] With comparable $\sigma_{\text{e}}^{\text{eff}}$ and $\sigma_{\text{ion}}^{\text{eff}}$ giving a high δ value, another reaction front from the current collector side will form, and, lastly, the reaction front on the separator side will diminish when $\sigma_{\text{ion}}^{\text{eff}} \gg \sigma_{\text{e}}^{\text{eff}}$ (Figure 4d). Considering that the here-employed composite possesses effective ionic and electronic conductivities of $(4.5 \times 10^{-3} \pm 0.5) \text{ mS cm}^{-1}$ and $(20 \pm 4) \text{ mS cm}^{-1}$, respectively (see the Supporting Information), the experimental results of operando neutron measurements, visualizing the reaction front from the separator side toward the current collector, agree well with theoretical prediction. The pristine cell, visualized here via neutron measurements, would correspond to $\delta \sim 2 \times 10^2$, predicting a severely uneven distribution of reaction current, as observed in the experiment. Details of the calculation are shown in the Supporting Information.

The presence of a reaction front propagating toward the current collector further implies an overlooked capacity loss mechanism in a thick composite cathode. A reaction rate distribution should be identical for both anodic and cathodic currents within the model, as long as the given parameters are unchanged (see Figure 4c,d). However, in practice, an effective ionic conductivity of the cathode composite experiences a substantial decrease upon delithiation above 2 V versus In/InLi (2.62 vs Li⁺/Li),^[8,31] leading to a gradient in lithium concentration in the thickness direction of the cathode composite. During the propagation of the reaction front from the separator side, the effective ionic conductivity of the composite decreases, and further delithiation from the current collector side will be hindered. Consequently, the lithium concentration gradient in the thickness direction remains after the recharging process, as observed in the in situ neutron tomography. This most likely accounts for the commonly observed asymmetric overpotential between discharge and charge after cycling.^[8] Exemplary asymmetric potential profiles of a solid-state Li–S battery with the same cathode composite are shown in Figure S7 in the Supporting Information. Irrespective of the nature of active materials, the slow ionic transport in composites has been shown in intercalation type solid-state batteries as well, suggesting that the here-found phenomena will also play a role in other types of solid-state batteries.

Therefore, a nonuniform reaction in the thickness direction caused by sluggish ion transport of the cathode composite highlights the necessity of 1) a processing procedure that does not sacrifice fast ion transport, 2) further development of solid electrolytes possessing both high ionic conductivity and electrochemical stability, and 3) a design principle of cathode architecture boosting the effective ionic conductivity. The third strategy includes the introduction of stable ion conductors and 3D structure design of cathode composite to establish a

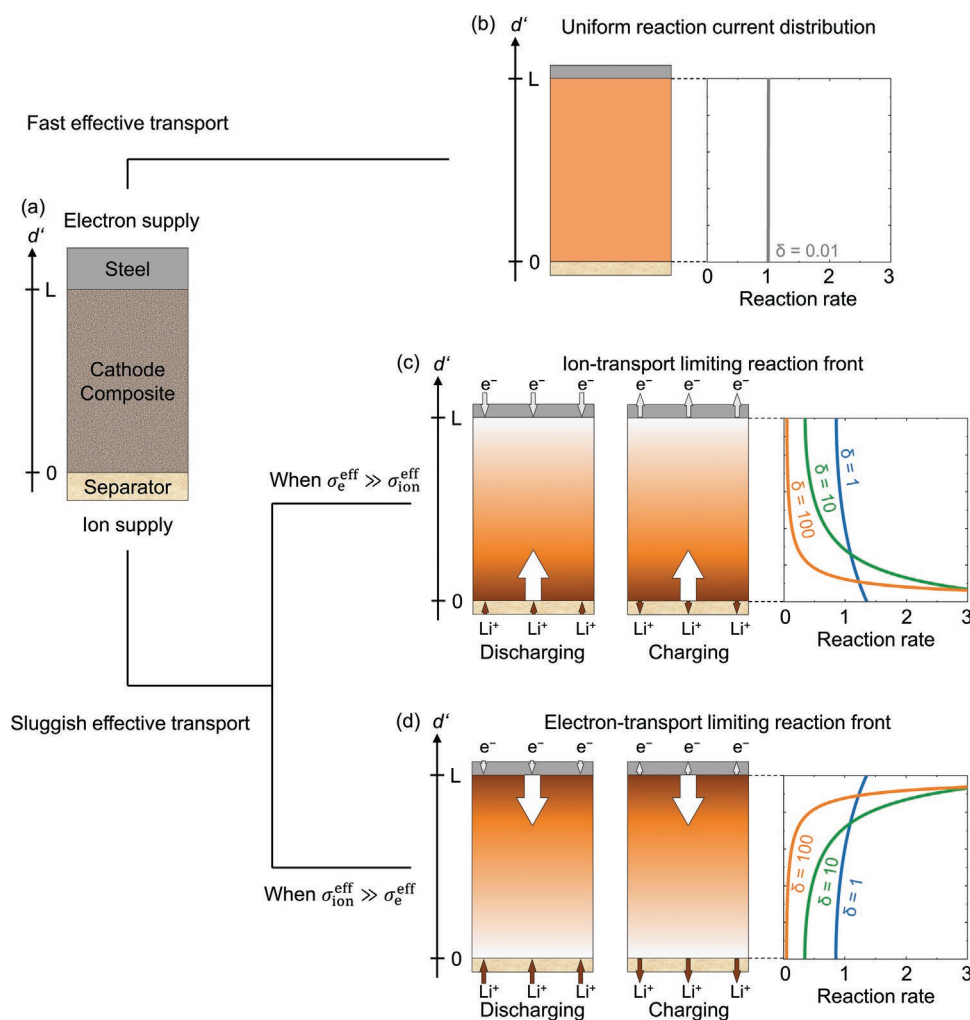


Figure 4. Extension of a porous electrode theory to solid-state sulfur cathodes. a) A schematic of the cathode composite with a thickness of L and an applied current of I . A δ parameter is given by $\delta \propto L|I| \left(\frac{1}{\sigma_{ion}^{eff}} + \frac{1}{\sigma_e^{eff}} \right)$. b) Porous electrode theory predicts a uniform reaction rate distribution with fast effective carrier transport. c) Sluggish ion transport within the composite leads to a nonuniform reaction rate, forming a reaction front propagating from the electrolyte-layer side toward the current collector. d) With low effective electronic conductivity, the reaction front propagates from the opposite side. The reaction rate distribution becomes less steep with lower δ by increasing the rate-limiting transport.

“highway” for ion transport within the composite, which further requires development of 3D transport modeling and visualization techniques with higher spatial resolution.

3. Conclusions

Operando neutron radiography and in situ neutron tomography have successfully been demonstrated and elucidate the transport limitations in a solid-state sulfur cathode composite. 2D radiographs reveal a reaction front, propagating from the separator-layer side toward the current collector upon the initial discharge. 3D tomography visualizes residual lithium concentrated in the vicinity of the current collector after recharging. Extending the porous electrode theory for solid-state batteries corroborates that the sluggish effective lithium-ion transport in composites is rate-limiting and leads to a nonuniform reaction front.

This work peeks into the lithium dynamics inside composite cathodes in solid-state batteries, showing that limitations exist in cathode composites due to slow ionic transport. Observing this reaction front urges further work in the design of cathode composites for solid-state batteries in general because high loading and thick cathode composites, as well as fast charging/discharging, are needed for realistic implementation of solid-state batteries.

Supporting Information

Supporting Information is available from the Wiley Online Library or from the author.

Acknowledgements

This research was supported by the Federal Ministry of Education and Research (BMBF) within the project LISZUBA under grant numbers

03XP0115A and 03XP0115C. S.O. gratefully acknowledges the Alexander von Humboldt Foundation for partial financial support through a Postdoctoral Fellowship.

Open access funding enabled and organized by Projekt DEAL.

Conflict of Interest

The authors declare no conflict of interest.

Author Contributions

I.M., W.G.Z., and S.O. designed the project toward the transport limitation. R.B., G.D., and S.O. designed the operando cell. G.D. and S.O. synthesized materials, prepared the cathode composites, and assembled the cells. R.B., G.D., T.A., and M.K. performed tomography. R.B. and N.K. analyzed the data. R.B., N.K., W.G.Z., I.M., and S.O. interpreted the data. R.B. and S.O. prepared the initial draft of the work. All authors gave comments and edited the manuscript.

Data Availability Statement

The data that support the findings of this study are available from the corresponding author upon reasonable request.

Keywords

composite electrodes, in situ neutron tomography, Li–S batteries, operando neutron radiography, solid-state batteries

Received: October 10, 2022

Revised: February 24, 2023

Published online: March 20, 2023

- [1] J. Janek, W. G. Zeier, *Nat. Energy* **2016**, *1*, 16141.
- [2] S. Randau, D. A. Weber, O. Kötz, R. Koerver, P. Braun, A. Weber, E. Ivers-Tiffée, T. Adermann, J. Kulisch, W. G. Zeier, F. H. Richter, J. Janek, *Nat. Energy* **2020**, *5*, 259.
- [3] D. Herbert, J. Ulam, *US Patent* | 3,043,896, **1958**.
- [4] X. Ji, K. T. Lee, L. F. Nazar, *Nat. Mater.* **2009**, *8*, 500.
- [5] X. Yang, J. Luo, X. Sun, *Chem. Soc. Rev.* **2020**, *49*, 2140.
- [6] S. Ohno, W. G. Zeier, *Acc. Mater. Res.* **2021**, *2*, 869.
- [7] G. F. Dewald, S. Ohno, J. G. C. Hering, J. Janek, W. G. Zeier, *Batteries Supercaps* **2021**, *4*, 183.
- [8] S. Ohno, C. Rosenbach, G. F. Dewald, J. Janek, W. G. Zeier, *Adv. Funct. Mater.* **2021**, *31*, 2010620.
- [9] S. Lorger, R. E. Usiskin, J. Maier, *Adv. Funct. Mater.* **2019**, *29*, 1807688.
- [10] C. Yu, S. Ganapathy, E. R. H. V. Eck, H. Wang, S. Basak, Z. Li, M. Wagemaker, *Nat. Commun.* **2017**, *8*, 1086.
- [11] B. Fan, Z. Guan, H. Wang, L. Wu, W. Li, S. Zhang, B. Xue, *Solid State Ionics* **2021**, *368*, 115680.
- [12] P. Minnmann, L. Quillman, S. Burkhardt, F. H. Richter, J. Janek, *J. Electrochem. Soc.* **2021**, *168*, 040537.
- [13] A. Bielefeld, D. A. Weber, J. Janek, *ACS Appl. Mater. Interfaces* **2020**, *12*, 12821.
- [14] F. Strauss, D. Stepien, J. Maibach, L. Pfaffmann, S. Indris, P. Hartmann, T. Brezesinski, *RSC Adv.* **2019**, *10*, 1114.
- [15] J. A. Lewis, F. J. Q. Cortes, Y. Liu, J. C. Miers, A. Verma, B. S. Vishnugopi, J. Tippens, D. Prakash, T. S. Marchese, S. Y. Han, C. Lee, P. P. Shetty, H.-W. Lee, P. Shevchenko, F. De Carlo, C. Saldana, P. P. Mukherjee, M. T. McDowell, *Nat. Mater.* **2021**, *20*, 503.
- [16] M. B. Dixit, J.-S. Park, P. Kenesei, J. Almer, K. B. Hatzell, *Energy Environ. Sci.* **2021**, *14*, 4672.
- [17] M. B. Dixit, W. Zaman, N. Hortance, S. Vujic, B. Harkey, F. Shen, W. Y. Tsai, V. De Andrade, X. C. Chen, N. Balke, K. B. Hatzell, *Joule* **2020**, *4*, 207.
- [18] D. P. Finegan, M. Scheel, J. B. Robinson, B. Tjaden, I. Hunt, T. J. Mason, J. Millichamp, M. Di Michiel, G. J. Offer, G. Hinds, D. J. L. Brett, P. R. Shearing, *Nat. Commun.* **2015**, *6*, 6924.
- [19] F. Sun, H. Markötter, I. Manke, A. Hilger, S. S. Alrwashdeh, N. Kardjilov, J. Banhart, *Appl. Surf. Sci.* **2017**, *399*, 359.
- [20] D. Goers, M. Holzapfel, W. Scheifele, E. Lehmann, P. Vontobel, P. Novák, *J. Power Sources* **2004**, *130*, 221.
- [21] M. Lanz, E. Lehmann, R. Imhof, I. Exnar, P. Novák, *J. Power Sources* **2001**, *101*, 177.
- [22] S. C. Nagpure, R. G. Downing, B. Bhushan, S. S. Babu, L. Cao, *Electrochim. Acta* **2011**, *56*, 4735.
- [23] X. Zhang, T. W. Verhallen, F. Labohm, M. Wagemaker, X. Zhang, T. W. Verhallen, F. Labohm, M. Wagemaker, *Adv. Energy Mater.* **2015**, *5*, 1500498.
- [24] T. W. Verhallen, S. Lv, M. Wagemaker, *Front. Energy Res.* **2018**, *6*, 62.
- [25] C. Wang, Y. Gong, J. Dai, L. Zhang, H. Xie, G. Pastel, B. Liu, E. Wachsman, H. Wang, L. Hu, *J. Am. Chem. Soc.* **2017**, *139*, 14257.
- [26] R. P. Rao, N. Sharma, V. K. Peterson, S. Adams, *Solid State Ionics* **2013**, *230*, 72.
- [27] V. F. Sears, *Neutron News* **1992**, *3*, 26.
- [28] S. Ohno, R. Koerver, G. Dewald, C. Rosenbach, P. Titscher, D. Steckermeier, A. Kwade, J. J. Janek, W. G. Zeier, *Chem. Mater.* **2019**, *31*, 2930.
- [29] J. S. Newman, C. W. Tobias, *J. Electrochem. Soc.* **1962**, *109*, 1183.
- [30] A. Neumann, S. Randau, K. Becker-Steinberger, T. Danner, S. Hein, Z. Ning, J. Marrow, F. H. Richter, J. Janek, A. Latz, *ACS Appl. Mater. Interfaces* **2020**, *12*, 9277.
- [31] G. F. Dewald, S. Ohno, M. A. Kraft, R. Koerver, P. Till, N. M. Vargas-Barbosa, J. Janek, W. G. Zeier, *Chem. Mater.* **2019**, *31*, 8328.